The Supernova Remnant Cas A at Millimeter Wavelengths

Melvyn Wright¹, John Dickel², Barron Koralesky³, and Lawrence Rudnick³

ABSTRACT

We used the BIMA array to map the supernova remnant Cas A from 28 to 87 GHz with 2" to 7" angular resolution. Data from 75 to 87 GHz, with 19 pointing centers were combined with single dish data to form a completely sampled image. These new BIMA images were compared with VLA images at 1.5 and 5 GHz to look for spectral index variations across Cas A. The images were spatially filtered and convolved to a common sampled uv-range corresponding to angular scales from 7" to 95". The images give direct evidence for a steeper spectral index in the knots outside the bright ring. Analysis of the 26 brightest peaks gives statistical evidence for spectral index variations throughout the remnant. The high frequency spectra confirm and extend the spectral variations seen previously at lower frequencies. The spectra are largely consistent with different power laws, and not curved spectra. This provides strong support for local variations in the acceleration of relativistic particles in Cas A.

Subject headings: SNR: individual (Cas A) — radio continuum: galactic — techniques: interferometric — ISM: supernova remnants — ISM: cosmic rays

1. Introduction

Cas A has been widely studied, both as a nearby (3.4 kpc, Reed etal 1995) example of a recent (AD 1680, Ashworth 1980) supernova within our Galaxy and also as a possible source of cosmic ray acceleration. Braun, Gull & Perley (1987) summarize the physical processes in Cas A as follows. In the simplest models, a Type II SNR such as Cas A ejects about 5 M \odot of material with velocities up to 10,000 km/s. Most of the energy is in a small (0.3 M \odot) component at the highest velocities. These ejecta create a blast wave which sweeps up interstellar material and slows to about 2300 - 3900 km/s with densities 0.4 to 4 cm⁻³. The more massive, slower ejecta are now interacting with this shocked material creating a turbulent shell which is seen as a bright, clumpy ring of radio emission with a radius of about 120" (2pc). A different model, where Cas A's shell is due to the interaction of the SN explosion with a pre-existing circumstellar shell, has been proposed by Chevalier & Liang (1989) and refined by Borkowski etal (1996).

Detailed multi-frequency maps of Cas A offer the possibility of studying the particle acceleration in a diffuse plasma. This acceleration is thought to take place in shocks in both galactic and extragalactic radio sources. The synchrotron spectral index traces the distribution of energy in relativistic particles. In a steady

¹Radio Astronomy Laboratory, University of California, Berkeley, CA 94720 E-mail: mwright@astron.berkeley.edu

²Department of Astronomy, University of Illinois, 1002 West Green Street, Urbana, IL 61801 E-mail: johnd@astro.uiuc.edu

³Department of Astronomy, University of Minnesota, 116 Church St SE, Minneapolis, MN 55455 E-mail: barron@astro.spa.umn.edu, larry@astro.spa.umn.edu

state, first-order Fermi acceleration will lead to power law spectra with a mean spectral index of -0.5 in the presence of strong shocks (see review by Blandford & Eichler, 1987). However, Cas A has a mean spectral index of about -0.77 (Baars etal 1977), the steepest of any known SNR. It appears that it may be flattening with time (Dent etal 1974), although this has been questioned (Hook, Duffett-Smith & Shakeshaft 1992). There are several ways to produce different spectral indices. If the shocks are initially weak, the spectra will be steeper than in the strong shock limit. In addition, the shocks can be weakened ("modified") by the backpressure of accelerated cosmic ray ions (Jones & Kang 1992). Radio spectra calculated for the electrons from these cosmic ray-modified shocks show a concave shape with a hardening toward higher energies (Reynolds & Ellison 1992). Green & Scheuer (1992) point out that, without continued acceleration, the highest energy electrons will decay most rapidly and there should be a break in the spectrum somewhere at high frequencies. Turbulent acceleration with secularly increasing magnetic fields such as discussed by Dickel etal (1993) and Jun etal (1996) have also been considered, and yield different spectra from first-order acceleration. Those spectra and the efficiency of acceleration depend on local plasma turbulence properties, (e.g., Borovsky and Eilek, 1986).

Most studies of Cas A have focussed on the bright knots, thus avoiding most of the difficulties associated with mapping large-scale structures, such as missing or distorted features from incomplete uv coverage or deconvolution errors. From a study of 304 compact knots, Anderson & Rudnick (1996) find variations in spectral index across Cas A over a range from -0.65 to -0.9. Steeper spectra are typically associated with features suggested to be bow shocks by Braun, Gull & Perley (1987), and other features seen outside of the main radio ring; flatter spectra are found in the ring and bright features within it. The spatial scales over which significant and reliable variations are detected range from less than 11" to greater than 80" but many smaller scale features are present and they may have different spectral indices as well. These results indicate a direct link between conditions in various parts of the remnant and the energy distributions of the relativistic particles.

Comparison of high-resolution images at the highest frequency possible with maps at lower frequencies can reveal more accurately where the high energy particles are being generated, help distinguish between the various models, and provide a fundamental test of theories of relativistic particle generation in shocks. In this paper we present images from 28 to 87 GHz obtained with the BIMA array⁴. We compare these new BIMA images with VLA⁵ images at 1.5 and 5 GHz at similar resolution to compute a spectral index distribution. This study increases the frequency baseline over which the spectra can be determined by over an order of magnitude.

2. Observations

Observations were obtained with the BIMA array (Welch etal 1996) at 28, 77, and 85 GHz (see Table 1). The primary beam of the 6.1-m diameter antennas is Gaussian with FWHM 6.73', 2.49' and 2.25' respectively at 28, 77, and 85 GHz. In order to accurately image the full 5' extent of the radio source we observed on a hexagonal grid of 7 pointing centers with 2.5' spacing at 28 GHz, and 19 pointing centers with 1' spacing at 77 and 85 GHz. BL Lac was observed as a phase calibrator at 25 to 30 min. intervals, after 2

 $^{^4\}mathrm{The}$ BIMA array is operated by the Berkeley-Illinois-Maryland Association under funding from the National Science Foundation

⁵The VLA array is an instrument of the National Radio Astronomy Observatory. The NRAO is a facility of the National Science Foundation, operated under cooperative agreement with Associated Universities, Inc.

complete cycles of 19 pointings with 35s observations at each pointing at 77 and 85 GHz, and 6 complete cycles of 7 pointings at 28 GHz. The antenna gains were determined from observations of planets at short antenna separations. All data were obtained in an 800 MHz bandwidth using a digital correlator with 256 frequency channels. The 28 GHz observations were single sideband with a system temperature between 40 and 60 K. The 77 and 85 GHz observations were obtained in both sidebands of the local oscillator (LO) with single sideband system temperature between 190 and 450 K. All system temperatures are scaled to outside the atmosphere.

Single dish data at 87 GHz were obtained using the NRAO 12m telescope using on-the-fly mapping in 1996 September. The single dish beam pattern was obtained by mapping Saturn using the same technique, with a small correction for beam broadening due to Saturn's $19.43 \times 17.36''$ size. Saturn moved less than 3'' during the mapping. The corrected beam size was determined to be $76.6 \times 72.4''$. Maps were made by RA scans at 25'' intervals and after all the data were combined into a single map, we subtracted linear baselines for each RA scan. The Saturn observations gave an antenna gain 31.7 Jy/K and an integrated flux density of 96.7 Jy for Cas A for an adopted planetary brightness 149 K.

Maps from the BIMA data were made with the MIRIAD software package (Sault, Teuben & Wright 1995; Wright & Sault 1993). The interferometer data were combined using a maximum entropy mosaicing algorithm (MEM) using the single dish image as a default image (Cornwell & Fomalont 1989; Sault, Staveley-Smith, & Brouw 1996). The single dish data were deconvolved using a Gaussian beam with FWHM $77 \times 72''$. The single dish image at 87 GHz was scaled by the mean spectral index and used in a joint deconvolution at 75 to 87 GHz. We first made images in each available sideband of the LO, i.e. five images with mean frequencies of 28.5, 75.2, 78.7, 83.1, and 86.7 GHz. Each image used multifrequency synthesis (MFS) with eight 100 MHz bands across the 800 MHz wide sideband to reduce the effects of bandwidth smearing over the large field of view, and combined the multiple pointing centers into a mosaiced image which has been corrected for the primary beam. The 75.2 and 78.7 GHz images showed structures which differed at the 20% level even after careful editing of the data. The deconvolved images were quite sensitive to the uv-coverage when different subsets of the data were included in the imaging. The uv-coverage is improved by combining both sidebands of the LO at 77, and at 85 GHz using MFS synthesis. Although the 28.5 and 85 GHz images were very similar, there were significant differences between these and the 77 GHz image. The 77 GHz image was still quite sensitive to different subsets of the data, even with both LO sidebands combined. This image was made using a single configuration of the BIMA array with 10 antennas (Table 1). We are obliged to acknowledge that an MFS, mosaiced image with 45 baselines, 16 frequency bands and 19 pointing centers may be inadequate to look for spectral index variations in a complex source structure like Cas A. We therefore combined the 77 and 85 GHz data into a single MFS, mosaiced image with mean frequency 83.1 GHz, 117 baselines, 16 frequency bands and 33 pointing centers.

The 1.5 GHz images were obtained using the VLA between 1994 March 25 and 1995 March 25, with an effective (integration time weighted) epoch 1994.75 at a mean frequency 1.51 GHz. The 5 GHz images were obtained using the VLA at frequencies 4.4149, 4.9851, 5.0850 and 4.6351 GHz between 1994 June 30 and 1995 March 25, with effective epoch 1995.0, and mean frequency 4.8 GHz. The primary beam of the 25m diameter VLA antennas is approximately Gaussian with a FWHM 29.3' at 1.5 GHz, and 9.2' at 4.8 GHz. These data are described in more detail by Koralesky & Rudnick (1998). Maps from the VLA data were made using MEM, with flat defaults. The use of single dish images or scaled 1.5 GHz images as defaults, did not significantly affect the flux densities on angular scales studied here.

3. Results

Figure 1 shows the maximum entropy image with a mean frequency 83.1 GHz. The convolving half-power beamwidth was $6.5'' \times 6.2''$. This image includes the single dish data, and samples spatial frequencies from zero to 72590 wavelengths. The 83 GHz image is very similar to the 1.5, 5 and 28.5 GHz images with the same angular resolution. Figure 2 shows the maximum entropy images at 1.5, 5, 28, and 83 GHz all convolved to a common resolution of 7''. The same structures are apparent at all 4 frequencies.

The spectral index of the integrated flux density is not well determined by these data. The total flux density at each frequency is not measured by an interferometer, and neither the integral over the maps nor the measured visibility flux density on the shortest baselines (which differ for each frequency) provide good estimates of the total. The flux density is determined mainly by the single dish observations, which we used as a default image in the MEM deconvolution at 83 GHz, and by the shortest interferometer spacings. Although we could adjust the total flux density by adding in a low resolution image from single dish data at each frequency or by scaling a more complete image at a lower frequency, these data are much better utilized to look for variations with frequency in the brightness distribution across the source. For this purpose we do not need the absolute flux density scale. Indeed, the analysis is simplified if we remove the overall spectral index (SI), and look for variations in the structure on scaled images at each frequency. Figure 3 shows the difference between pairs of images after scaling to the mean spectral index (here called α_0) over the image. The scale factors were determined for each pair using the MIRIAD task IMDIFF which finds optimum parameters (in a maximum likelihood sense) for making one image approximate another image. The parameters are an amplitude scale factor, dc offset, shifts in x and y direction and an expansion. For all pairs of images the shifts were less than 0.2'' and the dc offset and expansion less than 0.1%. The amplitude scale factor is determined globally and does not depend on any one feature, although similar values are obtained if we use the strongest peak to scale the images.

Significant large angular scale differences are apparent in these images. These may be a result of instrumental effects such as different uv-sampling, primary beam and pointing errors, calibration and image processing errors. Using the difference between pairs of images we can identify large angular scale errors which must be present in each of the images at 1.5, 5, 28, and 83 GHz. To avoid confusion from these errors, we performed spectral measurements only on small angular scales.

In order to evaluate the spectral index distribution accurately, we must match the data as closely as possible, not only in angular resolution but also in the spatial sampling of the images. One possibility is to compare completely sampled images at each frequency. For this we need complementary single dish data at each frequency which is not currently available. On the other hand, the SI of the knots and filaments may differ from that of the smoother background. In this case we probably don't want to compute the SI from completely sampled images, but rather obtain the SI separately for filaments and background. Accordingly, to study the small scale structures, we spatially filtered the data to a common range of spatial frequencies. Since the large scale errors at 83 GHz correspond to spatial frequencies derived from the single dish data, we limited the range of spatial frequencies to those observed directly with interferometers. The images were convolved with a function having a Gaussian taper at both high and low spatial frequencies since we wish to avoid images which are sensitive to the detailed uv-sampling at the edges.

Figure 4 shows maximum entropy images at 1.5, 5, 28, and 83 GHz each spatially filtered to the same common uv-range defined by a circular annulus from 1870 to 26500 wavelengths. The effective convolving beam includes structures from 7" to 95". These images were scaled to the mean spectral index over the image using IMDIFF, as above. The mean spectral index, determined from the amplitude scale factors for

each pair of images, corresponds to a spectral index, $\alpha_0 = -0.76$ to -0.79, where $S \propto \nu^{\alpha}$. We also made images with a convolving beam from 7" to 60" for comparison. The mean spectral index α_0 , for these images, corresponds to a spectral index, $\alpha_0 = -0.77$ to -0.81. Although we might attribute this steeper spectral index to the smaller scale structure, the spectra might also be steepened by the poorer atmospheric phase coherence on the long baselines at high frequency.

Figure 5 shows the difference between pairs of spatially filtered images, after scaling to the mean spectral index over the image. The contour interval is 9 mJy/beam at 83 GHz, and scales as $\nu^{-0.77}$. There are some common features on these images which we believe correspond to real spectral index variations across the source. Other features, which are not reproduced on each of the difference images may not be real. To determine the significance of the features on the difference images we need to consider the sources of errors on the images.

4. Imaging Errors

Image errors are usually described by the thermal noise level and by the dynamic range (the ratio of the peak brightness to the off-source RMS). More germane to the problem of looking for spectral index differences across Cas A, is the image fidelity, i.e. how well does the image represent the real source brightness distribution. In the process of *reducing* the data we re-calibrated and imaged Cas A many times. The RMS difference between these images was about 7 mJy/beam at 83 GHz ($1.5 \times$ the thermal noise) and 5 mJy/beam at 28 GHz ($10 \times$ the thermal noise). The off-source RMS on the spatially filtered images at 1.5 and 5 GHz is 11 and 9 mJy/beam, respectively. The off-source RMS is not well determined on the mosaiced images at 28 and 83 GHz. We will use these empirical estimates of the RMS in evaluating the results.

A number of systematic errors may affect the derived spectral index distributions: i) incomplete images from poor uv-coverage, ii) calibration and flux density scale errors, iii) alignment and temporal changes in the images, iv) primary beam and pointing errors, v) deconvolution errors, vi) polarization errors.

i) The convolved images in Figure 2 at 1.5, 5, 28, and 83 GHz are well sampled for structures on the scale of the individual clumps. These images are not well sampled on angular scales greater than about 3' corresponding to the shortest spacing, 475λ at 5 GHz, and 600λ at 28 GHz. The 83 GHz image depends on the single dish data for large angular scales. The spatially filtered images (Figure 4) at 1.5, 5, 28, and 83 GHz are well sampled for structures from 7" to 95". Although the sampling is not identical, the maps should be complete within these angular scales.

ii) The flux density scale at 28.5 and 83 GHz is tied to observations of planets. Flux density measurements at different observatories are typically consistent at the 10% level, with a worst error of 20%. At 85 GHz, the two sidebands, which are separated in frequency by 3 GHz, were independently calibrated; these images were consistent to within 10%. Since we determined the amplitude scale factors from the difference images, we have sidestepped the dependence on the flux density scale, but take encouragement from the agreement of the spectral indices derived from the amplitude scale factors, and the overall spectral index of Cas A (Baars et al 1977). Calibration errors can result in image errors and SI artifacts. The calibrator, BL Lac is sufficiently close to Cas A, that baseline errors are not important. Calibration errors in the measured visibilities. The errors in the image are reduced by the square root of the number of independent measurements. Assuming a 1-2 hour time scale for the calibration errors with two antenna configurations, gives around 1% errors in the images.

iii) The alignment of the images was constrained by interpolating the 1.5, 5 and 83 GHz image onto a template using the 28 GHz image. The phase centers for the BIMA and VLA observations differed by 0.8^{s} in RA and 1.7'' in DEC, but the data were imaged onto a common tangent point. The observed differences in the structure are not consistent with a simple rotation, expansion or shift of the images.

The expected proper motions and changes in source structure are also small compared with our resolution. The expansion rate for the bright ring is 0.06-0.15 % per year (Koralesky & Rudnick 1998), leading to maximum displacements of 0.5'' over the 3-year span of our observations. The position uncertainties are estimated to be about 1/10 of the angular resolution. The corresponding errors in the spectral index between 83 and 5 GHz are \pm 0.05 and \pm 0.35 at the peaks and 10% contours of the clumps respectively. In the analysis we will discuss only the bright peaks and clearly the spectral index on the steep edges of the clumps is to be treated with caution.

iv) The primary beam response at 28 GHz, was determined from observations of the radio source 3C454.3, with a flux density of approximately 8.7 Jy. The source was observed with a grid pattern of pointing offsets over 300" x 300", with 75" spacing, and over 360" x 360" with 90" spacing. The best fit Gaussians for the beam pattern were 386" x 380", and 382" x 379", respectively, with 1% to 2% residuals. We measured the primary beam response at 90.4 GHz using a transmitter which is installed at 7 degees elevation at a distance of 5 km. The antennas were focussed on the transmitter and scanned across the transmitter using the interferometer. The measured voltage primary beam pattern was interpolated out to 800" on a two dimensional grid with 48" spacing by using a second antenna as reference. Within the half-power points the primary beam response is well fitted by a Gaussian with FWHM 127" at 90.4 GHz, in good agreement with the Gaussian primary beam model used for mosaicing. Although the primary beams for both the BIMA array and the VLA are well determined, the primary beam models do not perfectly represent the actual primary beam patterns.

Figure 6 shows profiles of the measured voltage primary beam pattern of a BIMA dish using holography on a transmitter at 90.4 GHz (solid line). The dashed line shows the Gaussian model used in the image reconstruction, and the dot-dashed line shows the differences between the measurement and the model. Differences as large as 20% of the model occur within the 5% cutoff used in the image reconstruction. Beyond the 5% cutoff point, the real primary beam has sidelobes up to 5% in voltage (0.25% in power) which extend over the entire measured pattern. This sidelobe response is not included in the primary beam model used for mosaicing. The sidelobe response is unrepresented, and also contributes to amplitude errors in the visibility data. In an attempt to estimate the errors which might result from the difference between the primary beam model and the real primary beam pattern we made images using different primary beam models. These images differed at the 1% level.

Pointing errors also affect the amplitude of the visibility data. The RMS pointing errors are about 5'' in each axis. Although this is only 1/28 of the FWHM at 83 GHz, it gives 10% amplitude errors in the visibility data at the half-power points, and 20% errors at the 5% point of a Gaussian primary beam response. The errors at the 5% points are, of course, weighted down in the mosaiced image. The effect on the image fidelity depends on the source structure and on the time scale of the pointing errors. The source structure is extended, so that there is bright emission over most of the primary beam. The time scale of the pointing errors is around 1 hr. The errors in the image are reduced by the square root of the number of independent measurements. Assuming that all antennas have uncorrelated pointing errors results in 1% errors on the images.

v) Deconvolution errors can arise in several ways. A well known *feature* of maximum entropy

deconvolution is the enhanced resolution of high signal-to-noise ratio unresolved peaks in the image compared with lower brightness peaks. Note that we have compared images which have been convolved with a common Gaussian beam. We also made mosaiced images using subimages of different sizes. These mosaiced images differed by about 0.1%. The halo of emission around the shell in Figure 1 is an imaging artifact arising from the inadequate representation of the single dish beam by a Gaussian function. A better estimate of the single dish beam shape might be obtained by deconvolving the Saturn map using a model for Saturn, and allowing for the rotation of the beam on the sky. However, since we have spatially filtered out the large scale structure in deriving the Cas A spectra, the point is moot.

vi) The BIMA images were made with linearly polarized feeds. The resulting images are of the total intensity, together with an error term due to linearly polarized emission which is rotated by the parallactic angle at each sampled visibility. Cas A has a fractional polarization of 5% with an azimuthal E field when mapped at millimeter wavelengths at 1' angular resolution (Kenney & Dent 1985). We investigated the effect on the images using a model of Cas A with an azimuthal polarization pattern, with simulated mosaiced observations. The resulting images using linearly polarized feeds, which are sensitive to linearly polarized structure, differ from the true total intensity images by 0.6% RMS, with a maximum error of 2%. In addition, polarization leakage will contaminate the total intensity images at all frequencies at a typical level of 0.2%.

In summary, we expect that the images have errors at the 1% to 2% level, in agreement with the empirical estimates from the ensemble of images made using in the course of the data reduction.

5. Analysis of Spectral Index Variations

5.1. Direct evidence

The spatially filtered images provide direct evidence for spectral index differences for a few of the bright features. For example the clumps outside of the bright ring have a steeper spectral index than the mean spectral index α_0 , on each of the difference maps in figure 5.

We first look for spectral index variations on the difference maps because the noise is better defined than on spectral index maps involving a *ratio*. The hexagonal mosaic pattern used for the images at 28 and 83 GHz give a uniform sensitivity within a few percent over the entire image. The RMS noise level on the difference images is around 10 mJy/beam measured at 83 GHz, about 1 contour in Figure 5.

The flux density on the difference images is $\delta S = S - (\nu/\nu')^{\alpha_0} S'$, where S and S' are the flux densities at frequencies ν and ν' , and α_0 is the mean spectral index determined from the amplitude scale factor. For example, between 83.1 and 4.8 GHz, $\delta \alpha = 3.0 \times \delta S/S'$ for small values of $\delta S/S'$. i.e. all peaks > 1 Jy at 4.8 GHz with $\delta S < 10$ mJy/beam on the difference maps have $\delta \alpha < 0.03$. Thus the brightest feature on the difference maps, with $\delta S = -30$ mJy/beam and S' = 0.8 Jy gives $\delta \alpha = -0.11$.

In order to make reliable determinations of spectra in Cas A, we selected 26 distinct features that are readily identifiable on each of the four filtered images (Figure 7). The flux densities for the 26 components were determined by convolving the spatially filtered maps at each frequency by a 7" Gaussian beam centered on the 5 GHz peak. At a resolution of 7", we are averaging over much of the fine-scale structure studied, e.g., by Anderson & Rudnick (1996, AR96). However, they found that the largest variations in spectra occurred on large angular scales, so we assume that we are sampling the major spectral differences within the remnant.

The spectra for the 26 components are plotted in Figure 8, scaled by a spectral index -0.77 (Baars etal 1977), and normalized to 83 GHz. Fits to the 4-point spectral index range from -0.95 to -0.75. The spectral indices are listed in Table 2. The table lists non-linear least squares fits to the flux densities at 1.5, 5, 28, and 83 GHz. The average and RMS for the spectral index of the 26 components is -0.82 ± 0.05 The compact components are steeper on average than the integrated flux density. The steepest 7 spectra include the outer 5 compact components A, B, C, E, and R.

In order to test the robustness of these flux densities, we also measured them using a second, slightly different procedure. The 26 peak positions for each component were determined from the 5 GHz map. A box of 10" centered on each peak position was then searched in each of the other frequency maps and the peak flux density determined at each frequency. Both procedures allow for misalignments due to small structural changes or motions between the maps, but differ in the degree of large-scale filtering. Comparison of the flux densities for the 26 peaks between the two methods showed that the RMS deviation in derived spectral index was 0.015 between 1.5 and 5 GHz and 0.053 between 5 and 83 GHz.

Using the errors at each frequency as discussed in section 4, we find significant variations in spectral index among the 26 peaks. The range of spectral indices seen between 1.5 GHz and 83 GHz (-0.7 to -0.9) is similar to that seen between 1.5 GHz and 5 GHz, both here and as previously reported by AR96. The spectral indices between 5 and 28 GHz show a few points, typically with large errors, between -0.9 and -1.15; we believe these are spurious, reflecting the poorer coverage at 28 GHz, as discussed further below.

Since the centimeter and millimeter wavelength measurements were taken approximately two years apart, it is possible that changes in component flux densities over that period could distort the observed spectra. In order to estimate this, we determined the yearly fractional changes in the flux densities of our components using data from 1987 and 1994. We then used this to calculate the apparent changes in spectral index between 5 and 83 GHz that would be caused by such variations, if they continued at the same rate. The RMS change in spectral index was 0.013, much smaller than the component-to-component variations reported here, and thus not affecting any of our conclusions.

5.2. Color-Color plots

Another way to display the relationship between low and high frequency spectral indices for a collection of points is to plot them together in a scatter plot. Such a "color-color" diagram is shown in Figure 9. Diagrams such as this have been used to study spectral shapes for extragalactic synchrotron sources (e.g., Katz-Stone, Rudnick & Anderson 1993; Katz-Stone & Rudnick 1997)

There are a variety of advantages to using the color-color diagram. Spectra for a variety of locations in a source can be compared with one another in a single diagram. Small variations in spectral shape are easily detectable in color-color space. Flux density calibration errors at one frequency show up simply as a shift of all points in color-color space. Finally, and perhaps most important, if spectral variations are found within a source, one can tell whether these are all consistent with the same spectral shape.

The color-color diagram for the 1.5, 5, and 83 GHz data is shown in Figure 9. The errors on each point are the larger of (a) the formal 1-sigma errors due to the noise in the input maps or (b) one-half the difference between the spectral indices obtained by the two different peak flux density determination methods described above.

The low and high frequency spectral indices are clearly correlated with each other for the sample of 26

peaks. This confirms that the spectral variations seen between 1.5 and 5 GHz are also present up to 83 GHz, for the sample as a whole. This rules out mechanisms that produce curvature at the low end of the spectrum as explanations for the spectral variations discussed by AR96. We note that this is an ensemble conclusion. Individual points do deviate from a simple power law by as much as 0.1 in spectral index which could represent slight spectral curvature for some compact components, or other errors such as changes in component flux densities between the centimeter and millimeter observations. In addition, the data are clustered closely around the power-law line. The deviations from exact power-laws of different slopes are an order of magnitude smaller than would be expected even for models with minimal spectral curvature, such as those with a continuous injection of fresh electrons (e.g. Pacholcyzk, 1970). A continuous injection model with a low-frequency index of -0.75 is shown as the dotted line in Figure 9. The data are therefore not consistent with spectral variations in Cas A being due to a single electron population being sampled in different magnetic fields or having experienced different rates of high frequency losses. The most reasonable interpretation is that the data reflect different power-law slopes at different locations in the source; the chi-square for this model is 1.6 per degree of freedom (or 1.3, eliminating the worst point). The power laws extend at least from 1.5 GHz to 83 GHz; curvature beyond these limits is not probed.

The color-color diagram for the 1.5, 5, and 28 GHz data is not reliable, and is not shown here. There is a tendency for more points to fall below the power-law line than above, which could result either from losses steepening the high frequency spectra or from a bias towards low 28 GHz flux densities. Although many points still fall near the power-law line, there is a clear population far below the line. We do not believe these represent a reliable measurement of spectral shapes. If they did, then the corresponding points in the (1.5, 5, 83) GHz color-color diagram would have to fall even further below the power-law line, which they don't. We therefore attribute these deviations in the (1.5, 5, 28) GHz diagram to problems in the reconstruction of the 28 GHz map.

Most of the steepest spectrum components show a somewhat concave spectrum (see figure 8), which can also be seen in the color-color diagram as the group of points above the line. Such concave spectra are expected from cosmic-ray modified shocks (Reynolds & Ellison 1992). At present, we do not have a sufficient understanding of our errors to conclude that these deviations from exact power-law shapes are real. However, we note that if the millimeter wavelength flux density time variations are in the same sense, but more rapid than those at centimeter wavelengths, then such apparent curvature would be caused by our measurements being separated in time. Multi-wavelength observations at more closely spaced epochs are needed to isolate subtle spectral vs. temporal effects.

6. Discussion

In the previous section, we have established that the spectral variations seen at centimeter wavelengths in Cas A also extend at least to 3mm. In addition, the spectra show very little curvature over the range 1.5 GHz to 83 GHz, and are consistent with power laws with indices from -0.7 to -0.9.

Although the spectral variations in Cas A have been known for some time (Anderson etal 1991), until now it has not been possible to distinguish among the variety of possible physical causes. First, we can now rule out differential absorption by thermal ionized gas as the cause of these centimeter to millimeter wavelength spectral variations. Such absorption probably does affect the spectra at longer wavelengths (Kassim etal 1995). However, since the optical depth varies as $\nu^{-2.1}$, variations in spectral index over the range 0.2 between 1.5 and 5 GHz would translate only to a range 0.01 between 5 and 83 GHz, much smaller than is observed.

Another possibility is that the same very low frequency spectral index is found at all locations in Cas A (except for absorption), and that the spectral slopes at centimeter wavelengths are the result of high frequency breaks or other curvature in the spectra. One way to achieve this is through synchrotron losses, which are responsible for most of the spectral variations seen in extragalactic sources. The synchrotron lifetime at frequency ν GHz in a field B Gauss $\sim 1.6 \text{ B}^{-1.5} \nu^{-0.5}$ years. The estimated equipartition magnetic fields range from 1 to 5 mG in the bright knots giving a synchrotron lifetime 5000 to 500 years, at 83 GHz. Although the synchrotron lifetime at 83 GHz could lead to steepening of the spectrum at high frequency, the observed spectra do not show a spectral break. The synchrotron lifetimes at centimeter wavelengths are much longer than the age of the remnant, and cannot be the cause of steeper spectra in some locations. It is possible to construct scenarios in which the magnetic fields are higher than their minimum values, especially in the earlier phases of the SNR evolution, and caused significant losses to the electrons now radiating at centimeter wavelengths. Such scenarios are ruled out by the current observations, because they would lead to spectral shapes of much greater curvature than observed. In other words, for any reasonably shaped synchrotron spectrum with losses, the observed variations in the centimeter wavelength spectral indices should lead to much larger variations between centimeter and millimeter wavelengths than are observed.

We can also ask whether the observed spectra could be due to observing the electrons at different locations in different stages of the acceleration process, before they reach their asymptotic power laws. In such a picture, the electron energy distribution should cut off at high energies, where the particles have not had sufficient time to accelerate, or synchrotron or adiabatic losses occur on shorter timescales than the reacceleration (e.g., Blandford & Ostriker 1978; Volk & Biermann 1988). Detailed models with small diffusion coefficients (e.g. Kang and Jones 1991), can produce power laws over our limited frequency range of 30. But models with larger or energy-dependent diffusion coefficients lead to spectra which are too curved to be compatible with our observations, when the time scales for electron acceleration are comparable to the age of the accelerating shocks.

The remaining possibility is that the spectra at different positions represent the different power laws (at least over the 1.5 - 83 GHz range) resulting from slightly different local particle acceleration conditions. Such a scenario was discussed by Anderson & Rudnick (1996), who concluded that variations in external density and temperature could easily lead to variations in spectra of the observed magnitude, in a first-order Fermi accleration process where the spectral slope depends on the shock Mach number. However, they were unable to find a direct relation between dynamical properties of the compact features and their spectra. In fact, the spectral variations seen at centimeter wavelengths are not random from feature to feature, but are coherent over much larger scales, especially steepening outside of the bright ring. As argued by Anderson etal (1994), the particle acceleration may be regulated and vary over large scales (e.g., up to 1 pc), with compact features such as discussed in this paper representing regions of magnetic field amplification which then simply illuminate the background electron population.

We therefore conclude that the spectral variations observed at centimeter and millimeter wavelengths result from different local particle acceleration conditions in this complex and rapidly evolving young remnant. The relevant electron energies are $\approx GeV$. It is not yet clear what the limiting energy for these processes may be. Allen etal (1997) present evidence for a high energy X-ray tail in the spectrum of Cas A, which may represent synchrotron electrons of energies up to 4 x 10⁷ MeV.

The mean spectral index on the spatially filtered maps presented here is -0.77, the same spectral index

as the integrated flux density on the unfiltered maps. Since the spatially filtered maps contain only 18 ± 1 % of the integrated flux density on the unfiltered maps, we conclude that either acceleration occurred in very large scale features that are currently not visible, or particles accelerated in structures between a size range of 95" to 7" must diffuse throughout the entire remnant.

Since the spectral index is steeper than -0.5, under the shock acceleration model, the entire shell is decelerated - not just the features outside the bright ring, which are even more so. As argued by Anderson & Rudnick (1996), the clumps are brighter because of increased emission due to field amplification. Particle acceleration could also increase the emission, but compact features would then have different spectral indices than their local diffuse emission, which is not observed.

The steepest 7 spectra include the 5 compact components A,B,C, E, and R located outside the bright ring. The steepest spectrum fitted, $\alpha = -0.95 \pm 0.05$, was for feature C, which was found by Braun et al. (1987) to have the characteristic structure of a bow shock. The particle acceleration conditions are therefore different at the bright ring, and exterior to it, and consistent with the suggestion that these clumps may have been decelerated so that their low Mach number allows a steeper spectrum for the shock acceleration (Anderson & Rudnick 1966).

We performed some simple calculations to estimate how much homogenization of the electron populations might have occurred through spatial diffusion. We can think of diffusion as a stochastic process with a coherence time dt years. We estimate the diffusion using the Alfven velocity, $v_a = B/\sqrt{4\pi\rho}$. Using an equipartition magnetic field, B = 3 mG, and thermal density 2 cm^{-3} , then $v_a \sim 4000 \text{ km/s}$ (about the same as the current, decelerated knot velocity). Suppose that the electrons stream along ordered field lines at the Alfven velocity for a time dt years. The corresponding angular scale is $\sim 2 \times 10^{11} \times dt$ km (0.4 dt''). Assuming that the size of the smallest features resolved in Cas A at 15 GHz (Arendt & Dickel 1987) corresponds to the shortest scale length of the ordered magnetic field, then $dt \sim 1$ year. In the Cas A lifetime, ~ 300 years, electrons can diffuse over ~ $\sqrt{300/dt} \times 0.4'' \times dt \sim 7'' \times \sqrt{dt}$. Fluid turbulence will also spread out locally accelerated electrons further. Thus, we might expect to see spectral index variations on angular scales of $\sim 7''$ and larger if the particles were accelerated under differing physical conditions. Magnetic field enhancements from shocks and turbulence will create bright emission features which we see as knots and filaments (AR96). These features will have a spectral index corresponding to the underlying relativistic electron population. The magnetic field is not sufficiently coherent to allow diffusion of locally accelerated electrons over the entire remnant. Given major azimuthal variations in the dynamics (Koralesky et al., 1998), we are left with the conundrum of how the spectral index and apparently the electron distribution can be so similar over the large remnant. The same thing occurs in much larger objects, such as IC443.

7. Summary

1) The images of Cas A show the same structures at 1.5, 5, 28, and 83 GHz at 7" resolution.

2) The average spectral index for the 26 brightest peaks is -0.82 + -0.05, somewhat steeper on average than the integrated flux density (-0.77).

3) The spectra derived from images between 1.5 and 83 GHz show a range of spectral indices from -0.75 to -0.95. The data are most consistent with power laws of different slopes rather than curved spectra. The spectra between 1.5 and 83 GHz are consistent with no spectral break below 83 GHz in the clumps.

4) The five compact features outside the shell show significantly steeper spectra. The existence of different power laws at different locations demonstrates that particle acceleration varies across the remnant. Diffusion can smooth the electron distributions over scales on the order of our resolution (0.1 pc), but not throughout the entire remnant.

This work was supported in part by NSF Grant AST-9613998 to the University of California, and AST96-13999 to the University of Illinois. SNR research at the University of Minnesota is supported by the NASA Graduate Research Program and the National Science Foundation under grant AST 96-19438. We thank Mark Holdaway, Tom Jones, and an anonymous referee for comments which have improved the presentation of this work.

REFERENCES

- Allen, G.E., etal 1997, ApJ 487, L97
- Anderson, M.C., Rudnick, L., Leppik, P., Perley, R. & Braun, R. 1991, ApJ, 373 146
- Anderson, M.C., Jones, T.W., Rudnick, L., Tregillis, I.L., & Kang, Hyesung, 1994, ApJ, 421, L31
- Anderson, M. C. & Rudnick, L. 1996, ApJ, 456, 234
- Arendt, R. G. & Dickel, J. R. 1987, ApJ, 315, 567
- Ashworth, W. B. 1980, J. Hist. Astr., 11, 1
- Baars, J. W. M., Genzel, R., Pauliny-Toth, I. I. K., & Witzel, A. 1977, A&A, 61, 99
- Blandford, R.D. & Ostriker, J. P. 1978, ApJ, 221, L29
- Blandford, R., and Eichler, D. 1987, Phys. Rev., 154, 1
- Borkowski, K.J., Szymkowiak, A.E., Blondin, J.M. & Sazarin, C.L. 1996, ApJ, 466, 866
- Braun, R., Gull, S.F., & Perley, R.A. 1987, Nature, 327, 395
- Borovsky, J.E., & Eilek, J.A., 1986, ApJ, 308, 929

Cornwell, T. J., & Fomalont, E. B. 1989, in Synthesis Imaging in Radio Astronomy. ed. R. A.Perley, F.

- R.Schwab, & A. H.Bridle, ASP Conf. Ser. 6, 185
- Chevalier, R.A. & Liang, E.P. 1989, ApJ, 344, 332
- Dent, W. A., Aller, H. D., & Olsen, E. 1974, ApJ, 188, L11
- Dickel, J. R., Eilek, J., & Jones, E. M. 1993, ApJ, 412, 648
- Green, D. A. & Scheuer, P. A. 1992, MNRAS, 258, 833
- Hook, I.M., Duffett-Smith, P.J. & Shakeshaft, J.R. 1992, A&A, 255, 285
- Jones, T. W. & Kang, H. 1992, ApJ, 396, 575
- Jun, B.-I., Jones, T. W., & Norman, M. L. 1996, ApJ, 468, L59
- Kang, H. & Jones, T. W. 1991, MNRAS, 249, 439
- Kassim, N.E., Perley, R.A., Dwarakanath, K.S., & Erickson, W.C. 1995, ApJ Letters, 455, L59.
- Kenney, J.D., & Dent, W.A. 1985, ApJ, 298, 644
- Katz-Stone, D., Rudnick, L. & Anderson, M.C. 1993, ApJ, 407, 549.
- Katz-Stone, D. & Rudnick, L. 1997, ApJ, 488, 146.
- Koralesky, B., Rudnick, L., Gotthelf, E. & Keohane, J., 1998, ApJ (in press).
- Koralesky, B., & Rudnick, L. 1998, (in preparation)
- Pacholcyzk, A.G., 1970, Radio Astrophysics, (San Francisco: Freeman)
- Reed, J. E., Hester, J. J., Fabian, A. C., & Winkler, P. F. 1995, ApJ, 440, 706
- Reynolds, S. P. & Ellison, D. A. 1992, ApJL, 399, 75
- Rudnick, L. & Koralesky, B., 1998, preprint

Sault, R.J., Teuben, P.J., & Wright, M.C.H. 1995, A Retrospective View of Miriad, in: Astronomical Data Analysis Software and Systems IV, ed. R.A. Shaw, H.E. Payne & J.J.E. Hayes. PASP Conf Series 77, 433 (1995).

- Sault, R.J., Staveley-Smith, L. & Brouw, W.N. 1996, A&A Supp., 120, 375
- Schwab, F. R. & Bridle, A. H., ASP Conf. Ser. 6, 277
- Volk, H.J. & Biermann, P., 1988, ApJ, 333, L65
- Welch, W.J., Thornton, D.D., Plambeck, R.L., Wright, M.C.H., etal. 1996, PASP, 108, 93
- Wright, M.C.H. & Sault, R.J. 1993, ApJ, 402, 546

This preprint was prepared with the AAS ${\rm IAT}_{\rm E}{\rm X}$ macros v4.0.

Table 1: Observations

DATE	Frequency (GHz)	Telescope	uv-coverage (klambda)	
96SEP18	87	NRAO 12m	0 - 3.1	
96OCT16	83.1 - 86.6	BIMA 9-antenna c-array	1.9 - 36.3	
97JAN18	83.1 - 86.6	BIMA 9-antenna b-array	5.8 - 72.6	
97 SEP 02	28.5	BIMA 9-antenna c-array	0.6 - 6.7	
97 SEP 06	28.5	BIMA 9-antenna b-array	1.8 - 26.5	
97NOV29	75.2 - 78.7	BIMA 10-antenna c-array	1.5 - 20.7	

Table 2: Fitted Spectra

	Flux density at 1 GHz ^a	Spectral Index ^b
А	1.84	-0.83
В	2.77	-0.83
\mathbf{C}	4.03	-0.95
D	2.07	-0.85
Ε	5.07	-0.89
F	3.77	-0.75
G	2.32	-0.83
Η	1.73	-0.76
Ι	3.31	-0.78
J	3.76	-0.78
Κ	3.23	-0.76
\mathbf{L}	2.13	-0.82
Μ	3.90	-0.79
Ν	1.97	-0.79
0	2.34	-0.89
Р	2.11	-0.81
\mathbf{Q}	6.07	-0.85
\mathbf{R}	4.95	-0.92
\mathbf{S}	4.07	-0.86
Т	2.67	-0.79
U	2.26	-0.85
V	1.71	-0.75
W	2.83	-0.78
Х	3.44	-0.78
Υ	2.75	-0.81
Z	1.32	-0.78

 $^a\mathrm{The}$ errors in the flux density at 1 GHz are around 10 mJy.

 b The errors in the spectral index are estimated both from alternate measurements of the flux densities (see text), and from different weighting of the 4 frequencies range from 0.02 to 0.05.

8. Figure Captions

Figure 1. The maximum entropy image at 83 GHz convolved with a beam FWHM = $6.5 \times 6.2''$. This image contains the single dish data, and samples spatial frequencies from 0 to 72590 wavelengths. In this image and the subsequent maps, the coordinates are relative to the center of Cas A at RA 23:23:25.000 and Dec 58:49:00.000 (J2000).

Figure 2. The maximum entropy images at 1.5, 5, 28, and 83 GHz all convolved to a common resolution 7", and scaled to the mean spectral index over the image. The contour interval is 33 mJy/beam at 83 GHz. The synthesised beam FWHM is indicated by the filled ellipse in the lower left of each panel. The same structures are apparent in each images.

Figure 3. The difference between pairs of images after scaling to the mean spectral index over the image. (Top left 83-5 GHz, top right 83-28 GHz, bottom left 28-5 GHz, bottom right 83-1.5 GHz). The contour interval is 12 mJy/beam at 83 GHz. The synthesised beam FWHM is indicated by the filled ellipse in the lower left of each panel. Significant large scale differences are apparent. These may be a result of instrumental effects such as different uv-sampling, primary beam and pointing errors, and image processing errors.

Figure 4. Maximum entropy images at 1.5, 5, 28, and 83 GHz each spatially filtered to the same common uv-range defined by a circular annulus from 1870 to 26500 wavelengths. The effective convolving beam includes structures from 7" to 95". The images are scaled to the mean spectral index over the image. The contour interval is 21 mJy/beam at 83 GHz. The synthesised beam FWHM is indicated by the filled ellipse in the lower left of each panel.

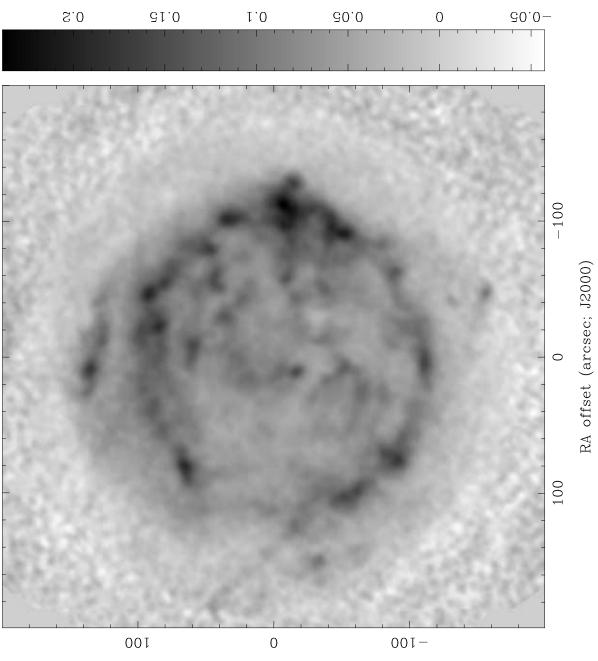
Figure 5. The difference between pairs of spatially filtered images, after scaling to the mean spectral index over the image. (Top left 83-5 GHz, top right 83-28 GHz, bottom left 28-5 GHz, bottom right 83-1.5 GHz). The contour interval is 9 mJy/beam at 83 GHz. The synthesised beam FWHM is indicated by the filled ellipse in the lower left of each panel. There are some common features on these images which we believe correspond to real spectral index variations across the source.

Figure 6. Profiles in position angles 0 and 90 degrees of the measured voltage primary beam pattern using holography on a transmitter at 90.4 GHz (solid line). The dashed line shows the Gaussian model used in the image reconstruction, and the dot-dashed line shows the differences between the measurement and the model.

Figure 7. The locations of 26 features which are readily identifiable at 1.5, 5, 28 and 83 GHz at 7" resolution. The contours show the spatially filtered image at 5 GHz. The contour interval corresponds to 240 mJy/beam at 83 GHz when scaled by a spectral index -0.77.

Figure 8. Spectra of the 26 features shown in figure 7 (two panels). The flux densities are scaled by a spectral index -0.77, and normalized to 83 GHz. The vertical, linear flux density scale is indicated at the bottom. The errors at each frequency are indicated at the top of the panel. Although most of the spectra are straight within the errors, the steepest spectra show a somehat concave shape (see section 5.2).

Figure 9. Color-color plots 1.5, 5 and 83 GHz. The solid line is the locus of power laws; 2 power law indicies are labeled for illustration. The dotted line shows a continuous injection model with a low-frequency index of -0.75. (see text)



DEC offset (arcsec; 12000)

